TECHNICAL PAPER

Wind tunnel and CFD analysis of dust re-emission potential from ground regions around successive stockpiles

B. Furieri[1] · C. L. de Morais[1] · J. M. Santos[1] · J.-L. Harion[2]

Abstract

Open industrial yards of granular materials can result in a large amount of particles emitted into the atmosphere due to wind erosion, offering risks to the environment and to the human health. It is important to estimate these emissions in order to manage dust control techniques and environmental polices requirements. There are several studies on particles emission from stockpiles surfaces, but there are few studies considering the re-emission that can occur from the regions around the stockpiles. Therefore, the present work aims to investigate the influence of the fluid flow complex structures near the ground region surrounding stockpiles and how they can influence the re-emission of particles. Experimental work using the oil-film technique and numerical simulations of the flow over one and two successive stockpiles oriented 30°, 60° and 90° to the incoming flow were performed. The results showed that a stockpile or successive stockpiles oriented 60° must be avoided in industrial sites as they promote high values of re-emitted mass around the piles. On the other hand, piles oriented 90° to the incoming flow showed the lowest re-emission potential for the surroundings. Finally, the gap between successive stockpiles showed insignificant influence on the emission estimates.

Keywords Computational fluid dynamics · Particulate matter · Air pollution · Steel industry

1 Introduction

Open industrial yards are widely used to storage granular material exposed to wind erosion that can cause particles emission into the atmosphere. In steel industry, for instance, large quantities of fine particulate matter of coal, iron ore and limestone are emitted from stockpiles to the atmosphere, offering risks to the environment and to human health [1–8]. To reinforce dust control techniques and environmental policies, it is necessary to estimate the amount of particles that can be emitted which depends on the local meteorology, the properties of the materials, and the way these materials are stored (shape and size of the stockpiles). The most widely used model for estimating particle emission from stockpiles in industrial sites was proposed by United Stated

Environmental Protection Agency [9]. Several numerical works have been carried out in order to improve this model by refining results of the shear stress distribution (or friction velocity distribution) over the stockpile surface [10–19].

However, there is still a lack in the literature concerning the emission that occurs around the stockpiles [20]. The particles around the piles may originate from the transport of material within the industrial site [21, 22] as well as from the stockpiles wind erosion characterized as re-emission, re-entrainment or resuspension phenomenon [23–27]. Therefore, the present work aims to continue the investigation initially carried out by Furieri et al. [20] by further analyzing the influence of fluid flow complex structures generating shear stress near the ground region surrounding successive stockpiles which is a more usual arrangement in industrial yards. In addition, the influence of the stockpiles orientation (regarding the prevailing wind direction) on re-emission is also investigated.

Technical Editor: Erick Franklin.

✉ C. L. de Morais
   cristinalimademorais@gmail.com

1   Department of Environmental Engineering, Universidade Federal do Espírito Santo, Vitória, ES 29075-910, Brazil

2   IMT Nord Europe Douai, 59500 Douai, France

2 The USEPA emission model

The United States Environmental Protection Agency emission model [9] proposes to estimate particles emission from stockpiles based on the erosion potential [g/m^2] as described in Eq. (1):

$$P = 58\left(u_* - u_{*t}\right)^2 + 25\left(u_* - u_{*t}\right) \tag{1}$$

where u_{*t} is the threshold friction velocity [m/s] at which the particle initiates its movement and u_* is the wind friction velocity [m/s] defined as $\sqrt{\tau/\rho}$, where τ is the shear stress and ρ is the density of wind. The threshold friction velocity u_{*t} can be measured or estimated and is dependent on the size and type of material considered [28–30]. On the other hand, the wind friction velocity u_* is estimated as given by an empirical expression described in Eq. (2).

$$u_* = 0.10 u_{10}^+ \left(u_s/u_r\right) \tag{2}$$

where u_{10}^+ is fastest mile (or gust) of reference anemometer [m/s], u_s is surface velocity measured at 25 cm from a real stockpile surface [m/s] and u_r is the wind velocity [m/s]. Equation (2) was obtained through the logarithmic wind velocity profile (see USEPA [9]) considering $z = 25$ cm and the surface rugosity, z_0, equal to a typical roughness height of 0.5 cm.

The model takes advantage of the subdivision of stockpiles surfaces into subareas to simplify the emission estimate. Areas with the same ratio u_s/u_r are considered as an individual diffuse source and the total emission (E) is the summation of the emission of each subarea M at each disturbance or perturbation event N (when material is added or removed from the surface) as given by Eq. (3).

$$E = k \sum_{i=1}^{N} \sum_{j}^{M} P_{ij} S_{ij} \tag{3}$$

where k is the particle sizer multiplier that represent the size of the emitted particles and S_{ij} is the area of the subarea considered [m^2].

Therefore, in the US EPA model, in addition to the threshold friction velocity, the friction velocity caused by the wind flow over the surface (either piles surface or the region surrounding the piles) is an important parameter to determine if the erosion will occur and at which magnitude.

3 Experimental work

The surface oil-film technique was used to investigate the fluid flow pattern over and around successive wood stockpiles surfaces. This experimental approach offers two-dimensional visualization with a good spatial resolution of the shear stress distribution associated to aeolian erosion. This technique consists in coating an oil mixture over a given wall exposed to flow friction. A thin layer of the mixture is coated over a surface around an object which the wall flow pattern is analyzed. Wind flow overpass the test section with oil-film mixture layer and creates some changes on its initial pattern. Due to friction forces, the wall flow features are then revealed, and color variation is directly linked to wall shear stress distribution on the coated surface.

The oil-film mixture used in this work had three components: (i) oil, (ii) small particles which are the solid part (yellow colored powder in the present work) and (iii) a chemical agent which allows the mixing between the others two components. As proposed by Desreumaux et al. [31], the paraffin oil was used as the oil part and the oleic acid as the mixing component. Several tests were performed to adjust the proportion of each component until the values that allowed the experiments to be carried out: 128 g/m^2 of paraffin oil, 5 g/m^2 of yellow dye and 23 drops/m^2 of oleic acid.

The experimental work was performed in the wind tunnel presented in Fig. 1. A photographic camera with resolution of 6 million pixels was placed right above the scaled-down successive stockpiles models in order to capture the oil movement according to the wind flow. The wood stockpiles placed in the wind tunnel were built considering the proportion of 1:200 relative to a full-scale coal stockpile (38° of angle of internal friction). Table 1 presents the stockpiles dimensions and the experimental cases. For all tested configurations, the free stream velocity of 6.5 m/s was used. Successive shots at each 15 min were taken until no significant modification between two consecutive photographs was identified. At this time, usually 5 h, the experiments were stopped. Details about wind flow stabilization and turbulence generation equipment as grids, honeycombs and ground roughness (represented by multiple small cubic obstacles) can be found in Furieri et al. [20] and Ferreira et al. [32]. It is important to point out that other configurations and conditions different from those presented in Table 1 were studied, but the oil technique did not reach any change that could be analyzed or linked to the fluid flow phenomenon around the stockpiles.

4 Numerical simulation

The three-dimensional equations of mass and momentum conservation for wind flow (fluid air with density and viscosity of 1.225 kg/m^3 and 1.789×10^{-5} kg/m s, respectively) over the stockpiles were solved using the software Ansys Fluent®, a solver based on the finite volume method. The chosen turbulent model was $k-\omega$ SST shear stress transport (SST), a two-equation model developed by Menter [33], that takes advantages of satisfactorily
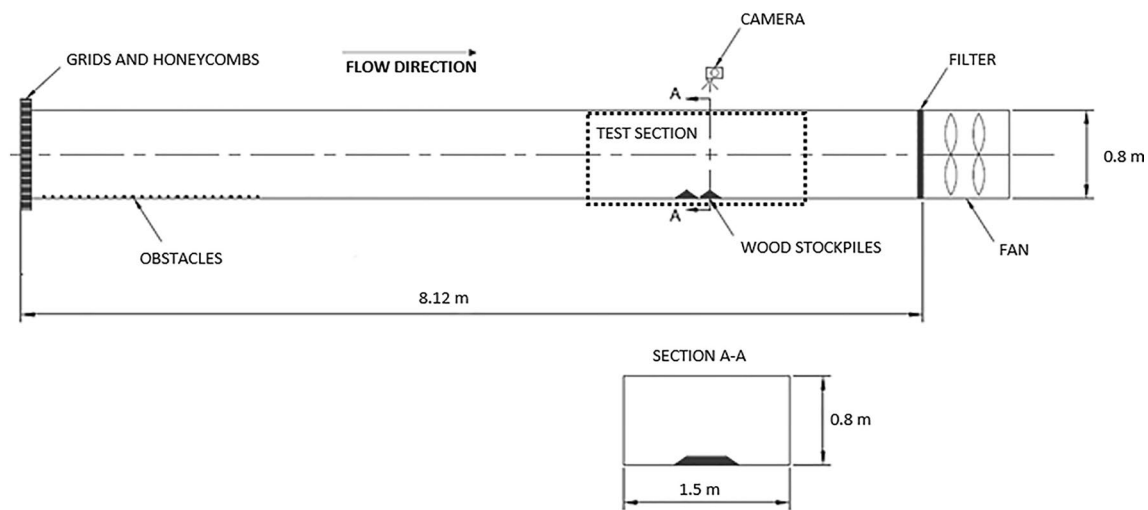
Fig. 1 Schema of wind-tunnel experimental setup (the dimensions are in meters)

Table 1 Experimental configurations investigated

Pile configuration and dimensions	Wind direction	Gap*	Free-stream velocity
	30°	1e	6.5 m/s
	60°	2e	
	90°	2e	

*The gap 1e is equal to 0.9h, where h is the stockpile height 0.080 m

modeling close to the wall using the $k-\omega$ model and away from the wall using the $k-\varepsilon$ model. The solution for momentum, turbulence kinetic energy (k) and its specific dissipation (ω) was obtained using the upwind second-order spatial discretization scheme. The SimpleC algorithm was used for the pressure–velocity coupling. The steady-state regime was also considered. Details of numerical choices can be found in previous work of similar simulations [18, 20, 32, 34–36].

Figure 2 shows the boundary conditions and the numerical domain. Two-dimensional vertical profiles of longitudinal velocity (u), turbulent kinetic energy (k) and dissipation rate (ω), obtained from previous simulations, were set up in the inlet conditions. At the top of the domain, the flow is considered undisturbed by the presence of the piles, as only half of the wind tunnel height (0.40 m) was considered in the simulation to reduce computational costs,

symmetry condition was applied. A boundary condition of fully developed flow (outflow condition) was set at the outlet of the computational domain, since the wind tunnel was not open to the atmosphere, not allowing a pressure condition to be set. In order to obtain results not influenced by the domain size, the geometry was built with sufficient distance upstream (8h, where h is the stockpile height of 0.080 m) and downstream (25h) the stockpiles, as can be seen in Fig. 2. Smooth walls with no-slip condition were set at lateral sides, ground and stockpiles walls.

The mesh was produced by extrusion of triangular cells defined on stockpiles walls and the ground surface. The size of the first wall cell was chosen to be at least $z^+ = 4$ in agreement to requirements by the use of turbulence model ($k-\omega$ SST) without any wall functions ($z^+ \leq 5$), producing a mesh of more than 5 million elements. Mesh sensitivity tests have

Fig. 2 Domain dimensions and boundary conditions. The origin of the domain is between the stockpiles. The coordinate x represents the streamwise direction, y represents the spanwise direction and z the domain height
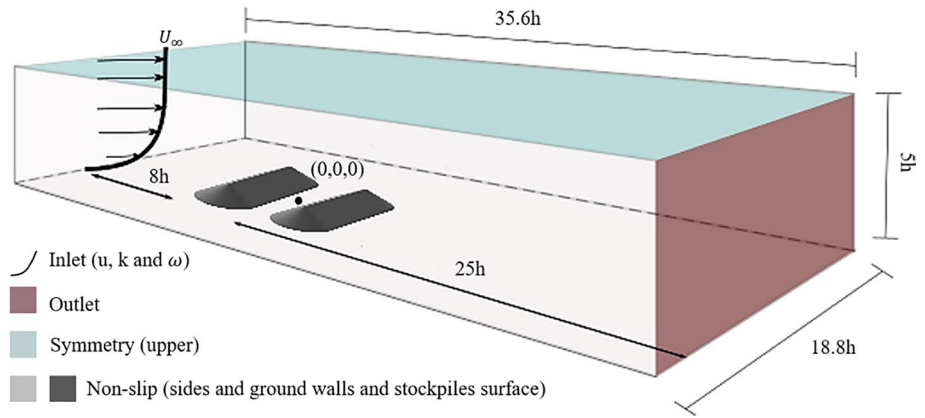
Table 2 Investigated scenarios using numerical simulations

Wind direction	Gap	Pile configuration	Free-stream velocity
30°	–	Isolated pile	6.5 m/s
	1e	Two successive piles	
	2e		
60°	–	Isolated pile	
	1e	Two successive piles	
	2e		
90°	–	Isolated pile	
	1e	Two successive piles	
	2e		

been previously carried out by Badr et al. [37] for the same configurations (Table 2).

5 Results

5.1 Air flow topology near the ground surrounding the stockpiles

Figures 3, 4 and 5 present numerical and experimental results for the configurations considering incoming flow perpendicular to the stockpiles (wind direction of 90°).

Figure 3a presents contours of normalized wall shear stress obtained by numerical simulations on the ground walls ($\tau_{ref} = 0.07$ Pa computed for the undisturbed region on the computational domain), and Fig. 3b shows the photograph taken when the oil-film pattern does not present more modifications during the experimental work. The acceleration regions are defined by the black arrows on the sides of the windward wall of the upstream stockpile. Furthermore, three regions are highlighted in this configuration: the main vortex A (region 1), the main vortex B (region 2) and a recirculation zone in the wake (region 3). The highlighted zones in these figures are very similar in both approaches showing

Fig. 3 Two successive stockpiles perpendicular to the incoming wind flow (direction 90°) with a gap equal to 2e: **a** Contours of non-dimensional wall shear stress magnitude obtained using numerical simulations and **b** photograph of oil-film surface flow on the ground region surrounding the two stockpiles
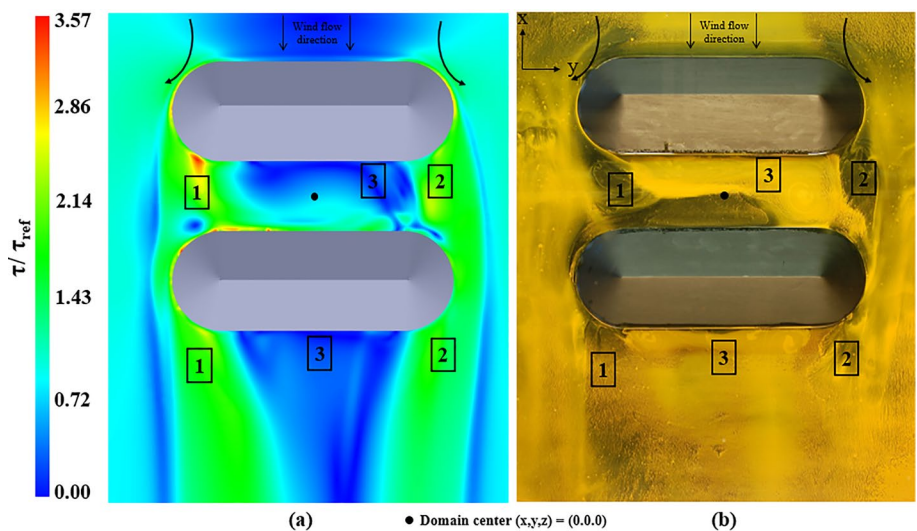
Fig. 4 Two successive stockpiles perpendicular to the incoming wind flow (direction 90°) with a gap equal to 2e: **a** Velocity vectors on a transversal (YZ) plane at x/h = 0 and **b** non-dimensional spanwise wall shear stress
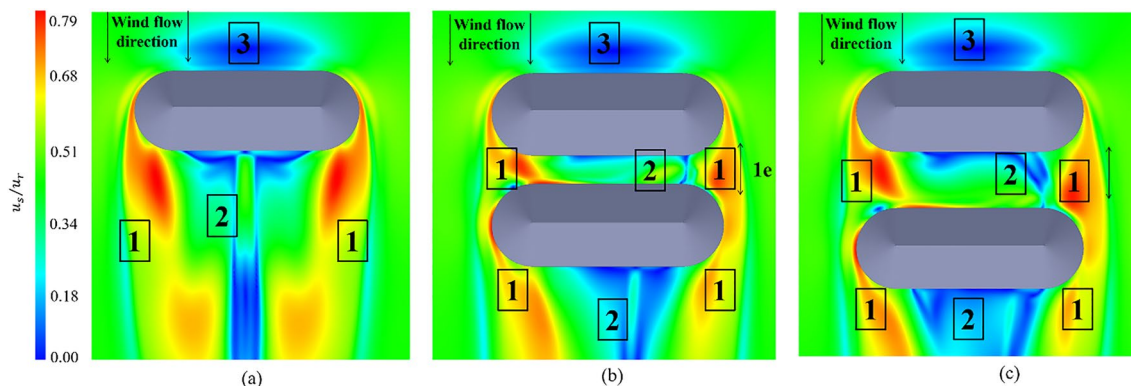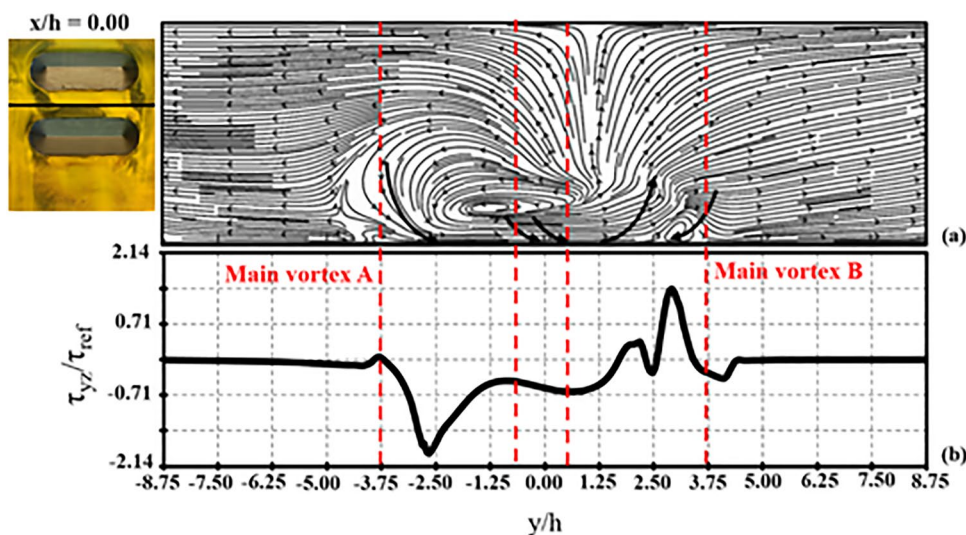

Fig. 5 Near wall flow distribution of u_s/u_r around two successive stockpiles perpendicular to the incoming wind flow (direction 90°): **a** isolated stockpile, **b** two successive stockpiles with 1e gap and **c** two successive stockpiles with 2e gap

good agreement between the experimental and numerical results.

The main vortex A presents stronger effects on the wall than the main vortex B. In addition, in the distribution of oil-film, the zone of intense black color is even more intense on the right side of the piles (region 1). This condition is caused by the bistability of the fluid flow around stockpiles. The zones of low wall shear stress shown by the numerical contours are well noticed on the photograph of experimental visualization (regions 3).

In Fig. 4, presenting the velocity vectors and spanwise wall shear stress evolution, the bistability of the flow is easily recognized. The velocity vectors show a large main vortex (vortex A) on the left and a smaller vortex (vortex B) on the right-hand side. The main vortex A presents a peak of $|\tau_{yz}/\tau_{ref}| = 2.14$ while the main vortex B expected to be symmetric presents the same peak equal to 1.43. The upwash

zone, normally placed in the middle line of the domain, is dislocated to the left (following the flow direction).

Finally, Fig. 5 shows the comparison of near wall flow distribution in terms of u_s/u_r for three arrangements: isolated pile, two piles with 1e gap and two piles with 2e gap. u_s/u_r is an important parameter for the USEPA emission model calculations. It is important to point out that, as mentioned before, the stockpile model was built with a proportion of 1:200 in relation to a real stockpile. So, u_s used in to analyze the erosion potential was 0.00125 m. Region 1 represents the effect of the main vortex A and B (Fig. 3). Region 2 downstream the first pile shows recirculation zones. However, the same region downstream the second pile, represents an ineffective zone with low levels of shear stress. Region 3 always describes an ineffective zone upstream de first stockpile. It can be noted that the arrangement containing two piles with 2e gap presents larger ground zones of low u_s/u_r and, consequently, zones of no take-off. The larger

the distance between the piles, the larger the ground zones of low u_s/u_r.

Figures 6, 7 and 8 present numerical and experimental results for the configurations considering the wind direction as 30° to the piles.

In Fig. 6, region 1 depicts the effects of the main vortex formed in the windward of the downstream stockpile on the ground surface. There is a strong friction on the wall in this region caused by the main vortex also identified in the photograph (knowing that the darkest regions indicate high wall friction and flow acceleration as the oil-film is dislocated towards another region on the plate). Region 2 is also an example of high friction on the wall as an effect of the main vortex formed downstream of the second pile. Regions 3, 4, 5 and 6 present an intense yellow color which indicate an accumulation of the oil-film corresponding in the

numerical results to low levels of wall shear stress. Regions 3 and 4 present the lowest levels of normalized wall shear stress (blue contours in Fig. 6a), and region 5 shows the impingement zone with low levels of wall shear stress. The incoming fluid flow is deviated towards the stockpile crest and lateral sides. The black arrows illustrate the flow acceleration perceived in this region: a local augmentation of the wall shear stress. Finally, region 6 shows an ineffective zone on the ground leeward the downstream pile on right of the main vortex while in the upstream pile, this region is concentrated between the piles.

The dashed lines in Fig. 6 delimit the effects areas of the main vortices on the wall: main vortex A formed on the upstream pile and main vortex B formed on the downstream pile which are also highlighted in Fig. 7. Figure 7 presents the evolution of the spanwise component of the

Fig. 6 Two successive stockpiles 30° to the incoming wind flow with a gap equal to 1e: **a** Contours of non-dimensional wall shear stress magnitude obtained using numerical simulations and **b** photograph of oil-film surface flow on the ground region surrounding the two stockpiles
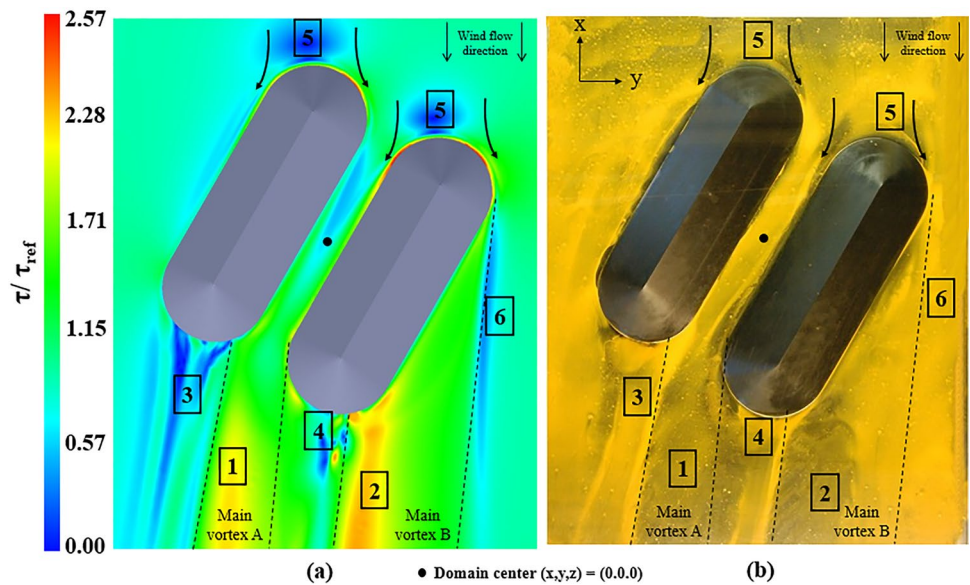

Fig. 7 Two successive stockpiles 30o to the incoming wind flow with a gap equal to 1e: **a** velocity vectors on a transversal (YZ) plane at $x/h = 6.25$ and **b** non-dimensional spanwise wall shear stress
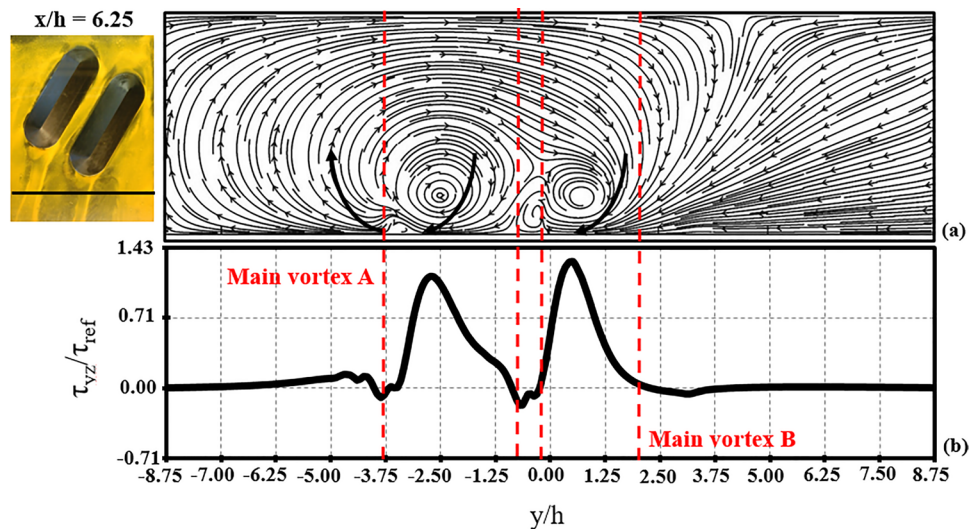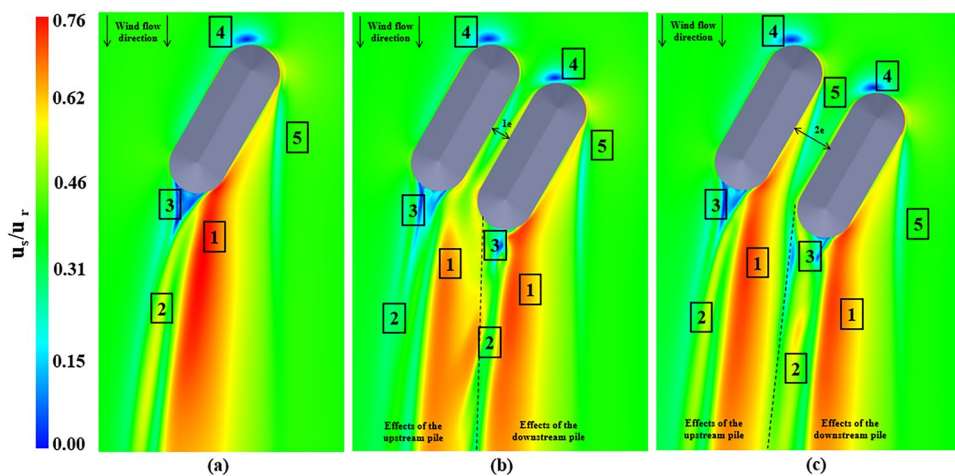
Fig. 8 Near wall flow distribution of u_s/u_r around two successive stockpiles 30° to the incoming wind flow: **a** isolated stockpile, **b** two successive stockpiles with 1e gap and **c** two successive stockpiles with 2e gap

wall shear stress and the velocity vectors on a YZ plane. Between the zones under the effects of the main vortices ($-3.75 < y/h < -1.25$ and $0.00 < y/h < 2.00$), there is a smaller vortex ($-1.25 < y/h < 0.00$) resulted from the modification of the main vortex A by the downstream pile. However, this smaller vortex does not present an important effect on the surface.

On the regions modified by the main vortices, downwash zones are noticed. These structures, highlighted over the velocity vectors, are responsible for high velocity gradient values near the wall which consequently results in high wall shear stress values ($\tau_{yz}/\tau_{ref} = 1.10$ for the main vortex A and $\tau_{yz}/\tau_{ref} = 1.31$ for the main vortex B). The peak of wall shear stress observed in the main vortex A is slightly smaller than the peak in the zone affected by the main vortex B caused by the interaction of the main vortex A with the downstream pile. In fact, the main vortex A does not impinge the downstream pile; however, it is slightly modified by its presence. Settled particles are re-emitted as a result of upwash zones. For instance, the velocity vectors in Fig. 7 show an upwash zone noticed at y/h approximately equal to -3.75. Accordingly, surface flow visualization shows at this transversal location an intense yellow color which is related to an accumulation of the coating.

Figure 8 shows the near wall velocity distribution, by the means of the ratio u_s/u_r, for the three tested arrangements. The pattern of the fluid flow distribution near the wall for the isolated stockpile (Fig. 8a) indicates five main zones: (i) region 1, effect of the main vortex, (ii) region 2, effect of the secondary vortex, (iii) region 3, ineffective zone downstream the pile (lowest levels of u_s/u_r), and (iv) region 4, wind flow impingement and (v) region 5, ineffective zone in the right of the main vortex. Figure 8b and c shows that some of these structures are strongly modified by the presence of a successive stockpile. In fact, only region 4 does not present significant differences. Figure 8b (gap 1e) indicates the contours of the main vortex on the near wall (region 1). The main vortex

is highly modified compared to the isolated configuration. A smaller area of the region 3 for the downstream pile (low levels of shear stress) is also noticed.

The results of wall flow topology around the piles are sensibly different between the three tested arrangements (isolated pile and successive piles with 1e and 2e gaps). The effects of the main vortex A (formed upstream) are highly modified by the downstream stockpile. Furthermore, in region 3, for the downstream piles, they are completely different in both configurations with two stockpiles, showing the influence of the distance between the piles.

Results for wind direction of 60° are presented in Figs. 9, 10 and 11. The configuration with a gap equal to 2e was chosen for this orientation to discuss numerical wall shear stress and oil-film fluid visualization. Among all the tested configurations, the effects noticed on the wall flow topology are the strongest for this orientation. In Fig. 9, four regions are highlighted: (i) region 1 is the effect of the main vortex formed on the upstream pile (main vortex A), and on the downstream pile (main vortex B), (ii) region 2 is the effect of the secondary vortex which is modified due to the presence of a downstream pile, (iii) region 3, the ineffective zone, indicates low levels of wall shear stress on the ground region situated between the main vortices, and (iv) region 4 is the impingement region.

It is worth to note that a very good agreement is observed between the visualizations shown in Fig. 9a and b. Region 1 presents the highest levels of normalized wall shear stress: a peak of approximately 4.30 is computed. The higher shear existent in the orientation 60° may be noticed comparing Figs. 9 and 6 (30°, maximal value: 2.57). Indeed, the zones of intense black color are greatly more visible for the orientation 60° (regions 1 in Fig. 9). Moreover, the equivalent region highlighted on the photograph has, as expected, an intense black color which means a zone of high friction over the surface. The main vortex strongly affects the velocity distribution in the wake. However, due to the presence of

Fig. 9 Two successive stockpiles 60° to the incoming wind flow with a gap equal to 2*e*: **a** Contours of non-dimensional wall shear stress magnitude obtained using numerical simulations and **b** photograph of oil-film surface flow on the ground region surrounding the two stockpiles
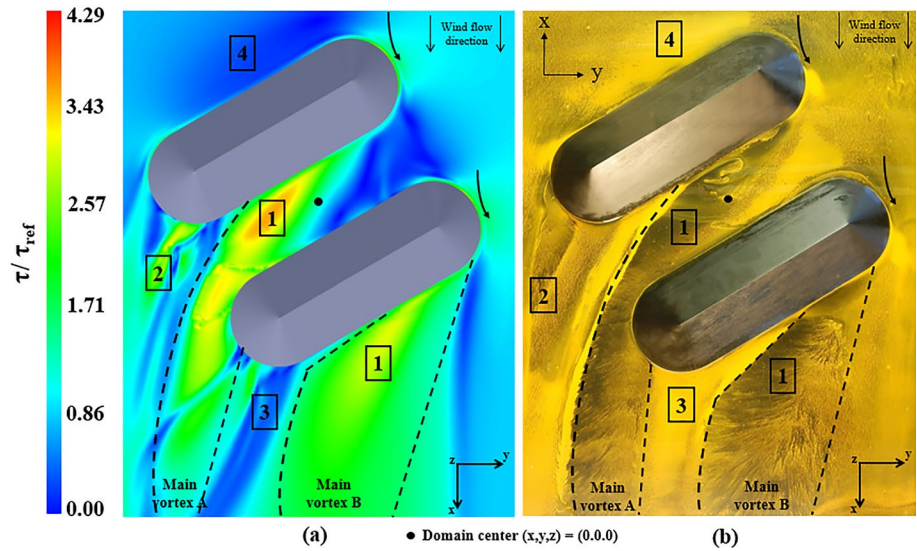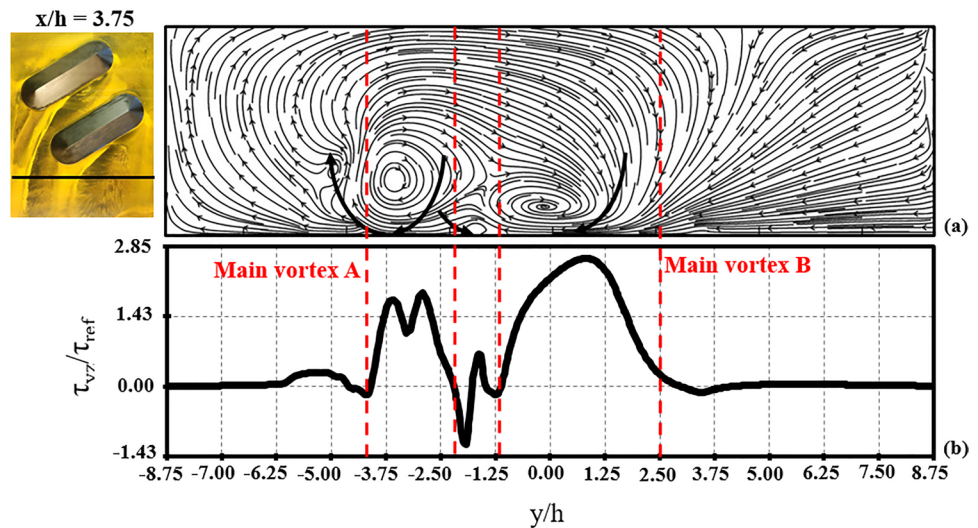

Fig. 10 Two successive stockpiles 60° to the incoming wind flow with a gap equal to 1*e*: **a** Velocity vectors on a transversal (*YZ*) plane at *x*/*h* = 3.75 and **b** non-dimensional spanwise wall shear stress

the second stockpile, the values of wall shear stress become more intense in the gap between the piles. The main vortex A is deviated by the downstream pile and intensifies the effects on the ground surface. Lastly, the main vortex B is similar to the structure formed around the isolated pile.

The important effects of the secondary vortex, which is a structure normally found in the isolated configuration, are not noticed in Fig. 9. Region 2 is the effect on the wall of a modified secondary vortex. The region 2 in the photograph shows small modification of the initial pattern of the oil-film. For the downstream pile, there is only the main vortex. The secondary one is replaced by the main vortex A, formed upstream. The photograph of the experimental technique shows, in region 3, an accumulation of the oil-film. The accumulation in this region is an expected pattern. This region is situated between the two main vortices, in a zone of very small wall friction. The numerical results also show

this pattern: the normalized wall shear stress over this region is less than the unity. The region 4 on the upstream pile does not present any modifications compared to the region seen in the isolated pile configuration. Additionally, the flow acceleration is equally observed in both piles and highlighted by the black arrows. Dashed lines on Fig. 10 delimit the regions of the effects of the main vortices A and B on the wake.

Details about the main vortices A and B, and their effects on the ground region responsible for the particle take-off, are illustrated in Fig. 10. Figure 10a depicts the velocity vectors over a spanwise plane. Figure 10b is a plot of the normalized spanwise component of wall shear stress. Both images are located at the same transversal position *x*/*h* = 3.75. Two main structures are highlighted in Fig. 11: main vortices A and B. Main vortex A is modified by the presence of the downstream stockpile. While main vortex B indicates a maximum value of shear stress
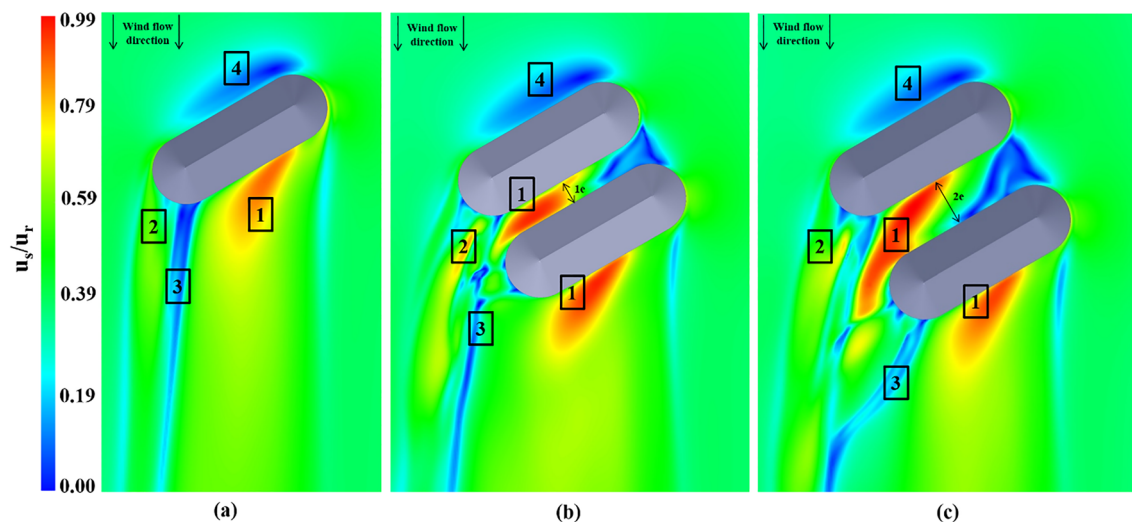
Fig. 11 Near wall flow distribution of u_s/u_r around two successive stockpiles 30° to the incoming wind flow: **a** isolated stockpile, **b** two successive stockpiles with 1e gap and **c** two successive stockpiles with 2e gap

$\tau_{yz}/\tau_{ref} = 2.60$, the peak for the main vortex A is smaller, about $\tau_{yz}/\tau_{ref} = 1.80$. Furthermore, in the right and left sides of the main vortex A smaller structures causing augmentations of the levels of τ_{yz}/τ_{ref} are noticed. The evolution of the spanwise shear stress of the main vortex B is about the same observed in the isolated stockpile. The black arrows represent upwash and downwash zones. The two peaks of normalized spanwise shear stress observed in Fig. 10a are linked to the downwash zones highlighted in Fig. 10b. Finally, there is an upwash zone for approximately y/h between −3.75 and 5.

Figure 11 shows numerical contours of u_s/u_r for all the tested arrangements of stockpiles oriented 60° to the wind flow direction. The four regions previously listed in Fig. 9 are highlighted in Fig. 11. The highest levels of u_s/u_r are found over the gap between successive stockpiles. As the piles are arranged with a larger gap (represented herein by the isolated stockpile), the effects of the main vortex on the ground are stronger. The fact of being nearby in the configuration 1e sensibly changes the main vortex A (formed on the upstream stockpile) which causes more impact on the stockpile surface than on the ground around the pile. The practical effects of these distributions will be discussed hereafter by the USEPA quantification of dust emissions.

5.2 Air flow topology near wall the stockpile surface

The main interest of this work consists in discussing the importance of the potential emission from the region around the piles relatively to the emission of the stockpiles

themselves. Therefore, it is necessary to calculate the of u_s/u_r distribution also over the stockpiles surface for all scenarios investigated in the present work. So, the emissions from the stockpiles surface and from the region around the piles can be both estimated.

Ferreira et al. [32] have already investigated the wall flow topology over an isolated pile and two successive piles (round crest) with different gap distances between the piles for the scenarios considering 60° and 90° wind direction relatively to the piles orientation. Furieri et al. [20] have also already investigated the wall flow topology over an isolated pile and two successive piles (sharp crest) with different gap distances between the piles for the scenarios considering 60° wind direction relatively to the piles orientation. Thus, the wall flow topology on the piles surface considering the scenarios concerned in the present work has been previously discussed in the literature, except the scenarios considering 30° and 90° wind direction orientation to piles with sharp crests. Therefore, these scenarios have been simulated to produce the of u_s/u_r distribution over the stockpiles surface (Figs. 12, 13) to be used to estimate the emission from the piles surface.

Figure 12a presents the near wall wind flow pattern for the isolated stockpile and shows high values of the ratio u_s/u_r near the crest with a maximum on the first detachment point, three zones with low values of u_s/u_r (impingement zone, upstream and on the bottom of the leeward wall) and traces of the main vortex on the leeward wall. Zone A indicated in Fig. 12a, b and c presents the differences found in u_s/u_r distribution for these three configurations. The other zones present very similar distributions: (i) the impingement region and the line along the crest both presenting the
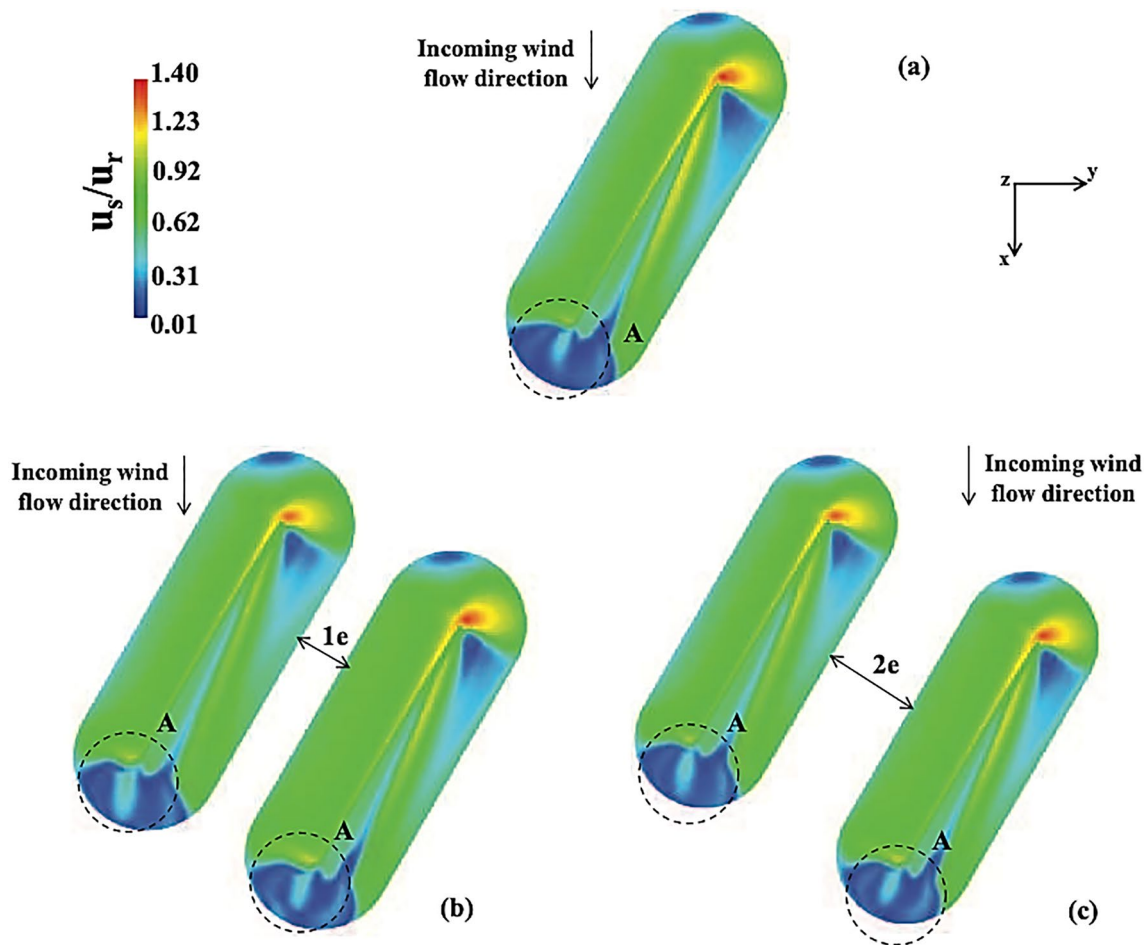
Fig. 12 Wind flow exposure on the stockpile oriented 30°: **a** isolated stockpile, **b** two successive stockpiles with gap 1*e* and **c** two successive stockpiles with gap 2 (with e = 0.9*h* where *h* is the stockpile height)

highest levels of the ratio u_s/u_r, (ii) an unaffected region on the leeward and windward wall and (iii) the effect of the main vortex on the leeward wall (high wall friction).

The isolated stockpile oriented 90° (Fig. 13a) presents the following main characteristics of the near wall velocity distribution: (i) the highest levels of u_s/u_r are found on the crest and on the sides of the piles, (ii) the recirculation zone downstream the pile causes the lowest levels of the ratio and (iii) on the lower part of the windward wall u_s/u_r values are near to zero and these values increase the top and sides. The analysis of the two nearby stockpiles leads to the identification of several zones of surface protection (low levels of u_s/u_r). Zone G in the leeward wall is more representative on the piles separated by the gap 1*e*. Also, the zones having high levels of u_s/u_r are smaller in these configurations. The analysis of the regions indicating the existence of ineffective zones over the wall, zone H shows up the differences on the near wall velocity distribution on the leeward wall. Here, on both piles it is increased the amount of surface with very low

levels of u_s/u_r. The formation of a large recirculation zone is the main cause of this behaviour on these walls.

As discussed in the previous section the near wall flow velocity for the 90° Wind direction scenario does not present a symmetric pattern as it is expected for RANS numerical simulations of geometrical symmetric configurations, indicated as bistability condition. Extra numerical simulations with stockpiles oriented 89.5° and 90.5° were simulated to further investigated this phenomenon (Fig. 14). The fluid flow pattern of 90° is very near the orientation 89.5° and the main vortex impinges the windward wall of the downstream pile on the same side (black dashed line). For the configuration 90.5°, this structure is observed on the opposite side. As the main aim of the present work is to quantify dust emission and the obtained results of dust emitted for the three orientations (90°, 90.5° and 89.5°) were lower than 3%, the dust quantified for 90° will be taken hereafter for the comparisons with 30° and 60°.
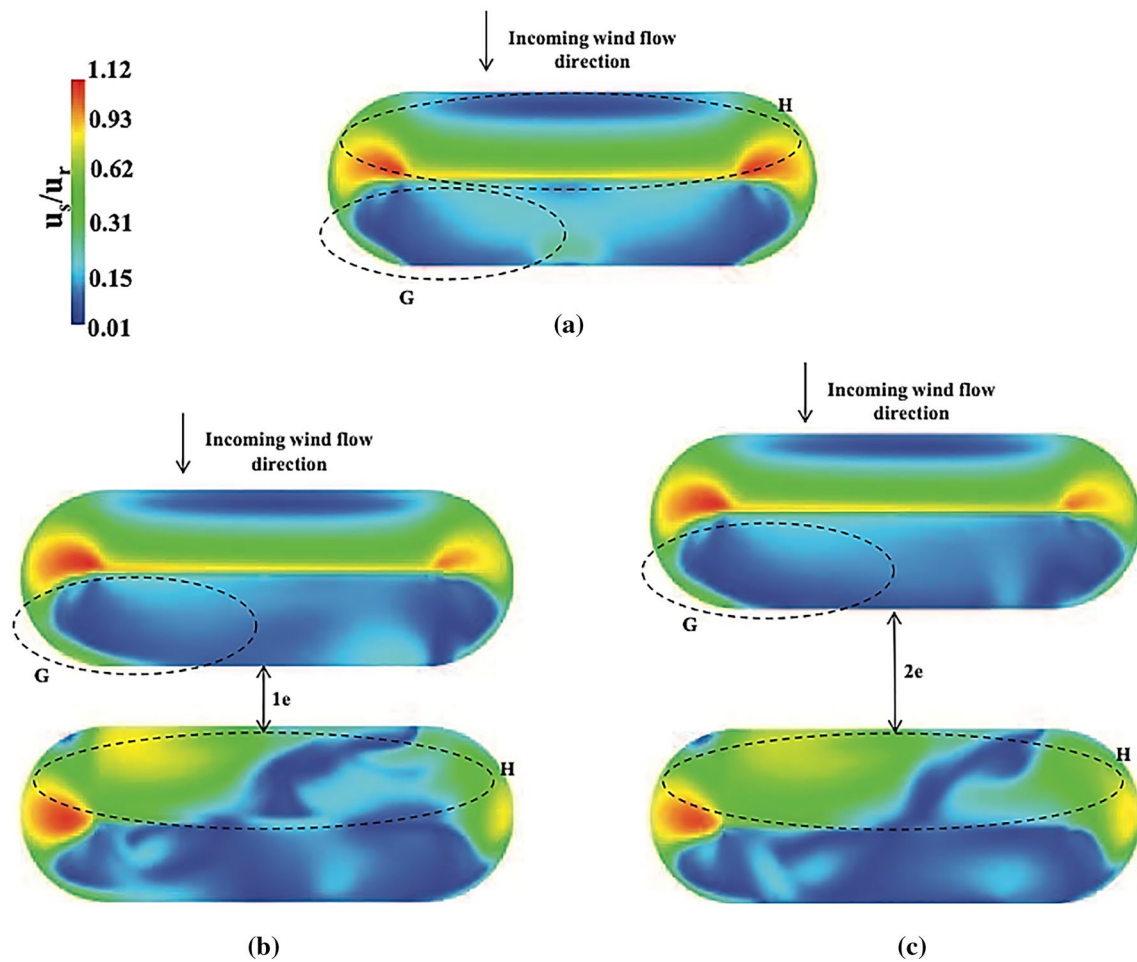
Fig. 13 Wind flow exposure on the stockpile oriented 90°: **a** isolated stockpile, **b** two successive stockpiles with gap 1*e* and **c** two successive stockpiles with gap 2 (with *e* = 0.9*h* where h is the stockpile height)
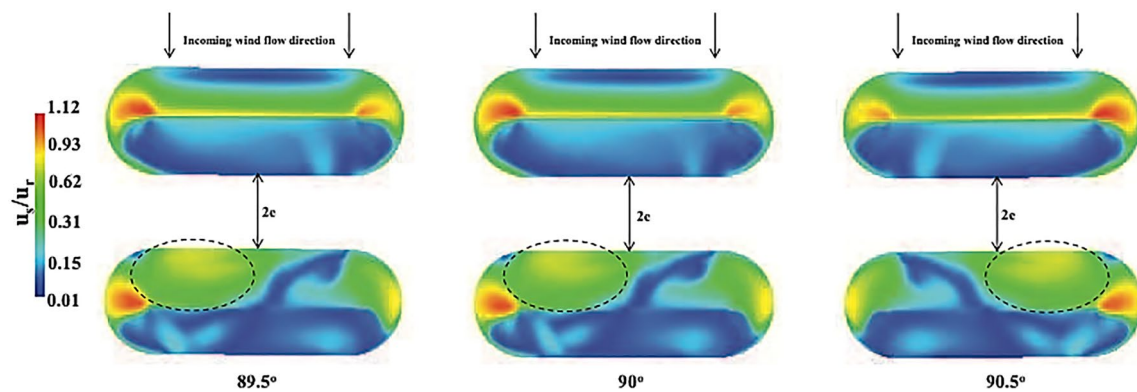

Fig. 14 Wind flow exposure on two nearby stockpiles with gap 2*e* oriented 89.5°, 90° and 90.5°

5.3 Dust emission quantification

The quantification of dust re-emissions on the surrounding areas of the stockpiles, as well as the emissions from piles surface, was carried out by using the USEPA methodology described in Sect. 2. The values of u_s/u_r distribution on the surfaces of the isolated pile and the successive piles with 1*e*

Table 3 Emission estimates by the USEPA model for free stream velocities of 5, 6.5, 10 and 15 m/s

Emissions [g]

	5 m/s					6.5 m/s					10 m/s					15 m/s				
	SEA [m²]	PEA [m²]	ESEA [g]	EPEA [g]	%	SEA [m²]	PEA [m²]	ESEA [g]	EPEA [g]	%	SEA [m²]	PEA [m²]	ESEA [g]	EPEA [g]	%	SEA [m²]	PEA [m²]	ESEA [g]	EPEA [g]	%
One pile 30°	0.025	0.036	0.017	0.090	19	0.124	0.089	0.196	0.338	58	0.600	0.106	2.851	1.573	181	1.271	0.128	14.834	4.649	319
Two piles 30° 1e	0.009	0.069	0.006	0.158	4	0.292	0.186	0.352	0.641	55	0.652	0.216	4.072	3.102	131	1.379	0.258	18.551	9.223	201
Two piles 30° 2e	0.026	0.070	0.017	0.158	11	0.327	0.186	0.444	0.641	69	0.720	0.216	4.670	3.099	151	1.430	0.258	20.347	9.216	221
One pile 60°	0.047	0.029	0.054	0.073	75	0.214	0.065	0.449	0.273	165	0.710	0.082	4.223	1.233	342	1.244	0.119	18.072	3.689	490
Two piles 60° 1e	0.081	0.102	0.153	0.301	51	0.320	0.161	0.815	0.965	84	0.861	0.191	6.074	3.788	160	1.524	0.250	24.245	10.734	226
Two piles 60° 2e	0.060	0.085	0.107	0.285	37	0.346	0.146	0.711	0.883	81	0.841	0.176	5.832	3.460	169	1.450	0.242	23.324	9.831	237
One pile 90°	0.021	0.024	0.014	0.056	26	0.129	0.042	0.212	0.204	104	0.579	0.052	2.851	0.870	328	1.251	0.098	14.562	2.570	567
Two piles 90° 1e	0.005	0.045	0.003	0.094	3	0.166	0.084	0.175	0.369	47	0.729	0.101	3.349	1.627	206	1.515	0.159	17.492	4.823	363
Two piles 90° 2e	0.010	0.045	0.006	0.088	7	0.170	0.091	0.207	0.370	56	0.799	0.108	3.667	1.678	219	1.581	0.161	18.724	4.995	375

SEA, surrounding erodible area; PEA, pile erodible area; ESEA, emission of surrounding erodible area; PEA, emission of pile erodible area

% = ESEA/EPEA

and 2*e* gaps for the wind flow oriented 60º were taken from the work of Furieri et al. [38].

The surface areas of interest surrounding the stockpiles were arbitrarily chosen (a distance equivalent to two stockpiles heights counting from the farther border of the piles in both direction—in the main wind direction and in the crosswind flow direction) for all configurations. Four free stream velocities were tested in the present analysis: 5, 6.5, 10 and 15 m/s. The tested stockpile was considered made of coal on both stockpile surface and the surrounding regions (threshold friction velocity equals 0.35 m/s according to Turpin et al. [15]). Table 3 compiles both the effective erodible areas and estimated emitted mass.

Table 3 shows, among several quantitative information, the increasing of wind velocity from 5 to 15 m/s increases the values of surrounding erodible area (SEA), pile erodible area (PEA), emission of surrounding erodible area (ESEA) and emission of pile erodible area (EPEA). As expected, when the tested free stream velocity increases the material threshold friction velocity is achieved for larger areas, resulting in larger emitted mass for all tested wind flow direction.

The incoming wind flow oriented 60° to stockpile presents the highest values of re-emitted dust on the surrounding areas for all tested velocities and gaps between successive stockpiles. In addition, up to 6.5 m/s, the major part of configurations presents larger emission from the pile compared to the stockpile surrounding area. On the other hand, for velocities higher than 6.5 m/s, for all cases, the surroundings are emitting more than the stockpiles with no distinction, being 90° the less emitting case considering the percentage analysis. However, analyzing the surroundings, the emitted mass for 90° cases has the lowest values than 30° and 60° cases. Finally, the gap between piles has only a much smaller influence on the analysis of dust re-emission and no trend is observed concerning all the tested cases.

6 Conclusions

The quantification of dust re-emission was not considered in any previous work concerning the aeolian erosion of successive diffuse sources. A complete analysis of the fluid mechanics of the incoming flow disturbed by the stockpiles arrangements has shown for all tested configurations air flow structures promoting zones of re-emission of settled particles.

The most important practical application is the comparative analysis of dust emission between different velocities, orientations, and arrangements. As the wind velocity increases the contribution of the area surrounding the piles also increases, which means that an increase in the wind velocity affects more strongly the emission around the piles than from the piles themselves. Also, in the cases where the

stockpiles were oriented 60° to the incoming flow, the surroundings' emitted mass was higher than the other cases for all tested velocities. Finally, the perpendicular orientation shown, for all configurations, the lowest emission estimates for the surroundings.

References

1. Tiwary A, Colls J (2010) Air pollution: measurement, modelling and mitigation, vol 47(8), 3rd edn. Routledge, New York. https://doi.org/10.5860/choice.47-4447
2. An Z, Jin Y, Li J, Li W, Wu W (2018) Particulate matter. Curr Allergy Asthma Rep 18(15):3–9. https://doi.org/10.1007/s11882-018-0768-8
3. Bové H et al (2019) Ambient black carbon particles reach the fetal side of human placenta. Nat Commun 10(1):1–7. https://doi.org/10.1038/s41467-019-11654-3
4. Hadley MB, Vedanthan R, Fuster V (2018) Air pollution and cardiovascular disease: a window of opportunity. Nat Rev Cardiol 15(4):193–194. https://doi.org/10.1038/nrcardio.2017.207
5. Miller MR (2020) Oxidative stress and the cardiovascular effects of air pollution. Free Radic Biol Med. https://doi.org/10.1016/j.freeradbiomed.2020.01.004
6. Seaton A, Tran L, Chen R, Maynard RL, Whalley LJ (2020) Pollution, particles, and dementia: a hypothetical causative pathway. Int J Environ Res Public Health 17(3):862. https://doi.org/10.3390/ijerph17030862
7. Sigaux J, Biton J, André E, Semerano L, Boissier MC (2019) Air pollution as a determinant of rheumatoid arthritis. Joint Bone Spine 86(1):37–42. https://doi.org/10.1016/j.jbspin.2018.03.001
8. Li X et al (2022) Air curtain dust-collecting technology: an experimental study on the performance of a large-scale dust-collecting system. J Wind Eng Ind Aerodyn 220(1):104875. https://doi.org/10.1016/j.jweia.2021.104875
9. USEPA (2006) 13.2.5 Industrial wind erosion. Compil Air Pollut Emiss Factors. https://doi.org/10.1130/0091-7613(1998)026%3c0363
10. Badr T, Harion JL (2005) Numerical modelling of flow over stockpiles: implications on dust emissions. Atmos Environ 39(30):5576–5584. https://doi.org/10.1016/j.atmosenv.2005.05.053
11. Badr T (2007) Quantification des émissions atmosphériques diffuses produites par érosion éolienne
12. Badr T, Harion J-L (2007) Quantification of diffuse dust emissions from open air sources on industrial sites. In: 3rd IASME/WSEAS international conference on energy, environment and sustainable development (EEESD '07). ISBN: 978-960-8457-88-1, no January, pp 276–280
13. Toraño JA, Rodriguez R, Diego I, Rivas JM, Pelegry A (2007) Influence of the pile shape on wind erosion CFD emission simulation. Appl Math Model 31(11):2487–2502. https://doi.org/10.1016/j.apm.2006.10.012
14. Diego I, Pelegry A, Torno S, Toraño J, Menendez M (2009) Simultaneous CFD evaluation of wind flow and dust emission in open storage piles. Appl Math Model 33(7):3197–3207. https://doi.org/10.1016/j.apm.2008.10.037

15. Turpin C, Harion JL (2009) Numerical modeling of flow structures over various flat-topped stockpiles height: implications on dust emissions. Atmos Environ 43(35):5579–5587. https://doi.org/10.1016/j.atmosenv.2009.07.047

16. Faria R, Ferreira AD, Sismeiro JL, Mendes JCF, Sousa ACM (2011) Wind tunnel and computational study of the stoss slope effect on the aeolian erosion of transverse sand dunes. Aeolian Res 3(3):303–314. https://doi.org/10.1016/j.aeolia.2011.07.004

17. Farimani AB, Ferreira AD, Sousa ACM (2011) Computational modeling of the wind erosion on a sinusoidal pile using a moving boundary method. Geomorphology 130(3–4):299–311. https://doi.org/10.1016/j.geomorph.2011.04.012

18. Furieri B, Russeil S, Harion J, Santos J, Milliez M (2012) Comparative analysis of dust emissions: isolated stockpile vs two nearby stockpile. WIT Trans Ecol Environ 157:285–293. https://doi.org/10.2495/AIR120

19. Derakhshani SM, Schott DL, Lodewijks G (2013) Dust emission modelling around a stockpile by using computational fluid dynamics and discrete element method. AIP Conf Proc 1542:1055–1058. https://doi.org/10.1063/1.4812116

20. Furieri B, Russeil S, Harion JL, Turpin C, Santos JM (2012) Experimental surface flow visualization and numerical investigation of flow structure around an oblong stockpile. Environ Fluid Mech 12(6):533–553. https://doi.org/10.1007/s10652-012-9249-0

21. Kia S, Flesch TK, Freeman BS, Aliabadi AA (2021) Atmospheric transport over open-pit mines: the effects of thermal stability and mine depth. J Wind Eng Ind Aerodyn 214(May):104677. https://doi.org/10.1016/j.jweia.2021.104677

22. Du C, Wang J, Wang Y (2021) Study on environmental pollution caused by dumping operation in open pit mine under different factors. J Wind Eng Ind Aerodyn 226(December 2021):105044. https://doi.org/10.1016/j.jweia.2022.105044

23. Balladore FJ, Benito JG, Uñac RO, Vidales AM (2020) Mineral dust resuspension under vibration: onset conditions and the role of humidity. Particuology 50:112–119. https://doi.org/10.1016/j.partic.2019.07.005

24. Bogacki M, Mazur M, Oleniacz R, Rzeszutek M, Szulecka A (2018) Re-entrained road dust PM10 emission from selected streets of Krakow and its impact on air quality. E3S Web Conf 28:1–10. https://doi.org/10.1051/e3sconf/20182801003

25. Patella V et al (2018) Urban air pollution and climate change: 'The Decalogue: Allergy Safe Tree' for allergic and respiratory diseases care. Clin Mol Allergy 16(1):1. https://doi.org/10.1186/s12948-018-0098-3

26. Gulia S, Goyal P, Goyal SK, Kumar R (2019) Re-suspension of road dust: contribution, assessment and control through dust suppressants—a review. Int J Environ Sci Technol 16(3):1717–1728. https://doi.org/10.1007/s13762-018-2001-7

27. Islamov RS (2020) Analysis of the dynamics of dust reentrainment with simultaneous electrostatic deposition and without any deposition after a jump of airflow velocity. J Aerosol Sci 144(October 2019):105533. https://doi.org/10.1016/j.jaerosci.2020.105533

28. Iversen JD, White BR (1982) Saltation threshold on Earth, Mars and Venus. Sedimentology 29:111–119

29. Foucaut JM, Stanislas M (1996) Take-off threshold velocity of solid particles lying under a turbulent boundary layer. Exp Fluids 20(5):377–382. https://doi.org/10.1007/BF00191019

30. Shao Y, Lu H (2000) A simple expression for wind erosion threshold friction velocity. J Geophys Res 105:22437–22443. https://doi.org/10.1029/2000JD900304

31. Desreumaux O, Bourez JP (1989) Préparation de bouillies pour visualisation pariétales sur maquette de sous-marin à cepra 19, France

32. Ferreira MCS et al (2020) Experimental and numerical investigation of building effects on wind erosion of a granular material stockpile. Environ Sci Pollut Res 27:14

33. Menter FR (1994) Two-equation eddy-viscosity turbulence models for engineering applications. AIAA J 32(8):1598–1605. https://doi.org/10.2514/3.12149

34. Furieri B, Santos JM, Russeil S, Harion JL (2014) Aeolian erosion of storage piles yards: contribution of the surrounding areas. Environ Fluid Mech 14(1):51–67. https://doi.org/10.1007/s10652-013-9293-4

35. De Morais CL, Ferreira MCS, Santos JM, Furieri B, Harion JL (2018) Influence of non-erodible particles with multimodal size distribution on aeolian erosion of storage piles of granular materials. Environ Fluid Mech. https://doi.org/10.1007/s10652-018-9640-6

36. Ferreira MCS et al (2019) An experimental and numerical study of the aeolian erosion of isolated and successive piles. Environ Fluid Mech. https://doi.org/10.1007/s10652-019-09702-z

37. Badr T, Harion JL (2007) Effect of aggregate storage piles configuration on dust emissions. Atmos Environ 41(2):360–368. https://doi.org/10.1016/j.atmosenv.2006.07.038

38. Furieri B, Harion J-L, Santos JM, Milliez M (2012) Comparative analysis of dust emissions: isolated stockpile vs two nearby stockpiles. Air Pollution XX 157:285–294